European Journal of Mechanics / A Solids 94 (2022) 104534

Contents lists available at ScienceDirect

European Journal of Mechanics / A Solids

journal homepage: www.elsevier.com/locate/ejmsol

# Structural and material electro-mechanical instabilities in microstructured dielectric elastomer plates

Marzieh Bahreman [a,b], Nitesh Arora [b], Hossein Darijani [a], Stephan Rudykh [b,c,*]

[a] Department of Mechanical Engineering, Shahid Bahonar University of Kerman, 76175-133, Iran
[b] Department of Mechanical Engineering, University of Wisconsin-Madison, Madison, WI53706, USA
[c] School of Mathematical & Statistical Sciences, National University of Ireland Galway, Galway, Ireland

ARTICLE INFO

*Keywords:*
Instabilities
Dielectric elastomer
Plates
Soft materials
Hyperelasticity

ABSTRACT

In this paper, we investigate the stability of microstructured dielectric elastomer (DE) plates under electro-mechanical finite deformations. We examine the influence of the DE composite microstructure parameters on the stability of the DE composite plate. In particular, we analyze the DE plates made out of laminated ideal dielectric phases. We use an exact solution for the incompressible DE laminates to determine the effective material behavior of the composite plates. The corresponding micromechanics-based energy density functions are used in the subsequent analysis of the DE plate stability. The unstable domains for different materials compositions, volume fractions, and properties of the DE composite phases are determined. Finally, we compare these results for the onset of structural instabilities in DE plates with the material instabilities predicted based on the loss of ellipticity analysis.

## 1. Introduction

Dielectric elastomers (DEs) belong to a class of soft active materials that undergo large deformations when excited by an external electrical stimulus (Pelrine et al., 1998, 2000a). Owing to their exceptional properties – quick response, lightweight, low cost, high energy density (Carpi et al., 2010; Suo, 2010), they became an attractive candidate for numerous applications, including soft robotics and actuators (Carpi et al., 2007; Gu et al., 2017), energy harvesters (Koh et al., 2010), resonators (Li et al., 2012), artificial muscles (Brochu and Pei, 2012), tunable waveguides (Galich and Rudykh, 2017; Gei et al., 2010), braille display (Chakraborti et al., 2012), optical components (Fang et al., 2010), and prosthetic limbs (Biddiss and Chau, 2008). A typical setup of the DE actuator consists of a thin elastomer membrane sandwiched between two compliant electrodes. When the voltage is applied across the electrodes, the elastomer film contracts in the thickness direction and expands in the lateral directions. It has been reported that voltage-induced actuation strains in DE actuators can reach well beyond 100% (Pelrine et al., 2000b).

The major limitation of DE applications is that they require extremely high electric voltage to produce relevant actuation strains. Some approaches to overcome the limitation have been proposed, including utilizing electro-mechanical instabilities (Keplinger et al., 2012; Rudykh et al., 2012) or modulating the waveform of input voltage (Arora et al., 2018). However, the former approach requires the operation of DE actuators in the risky vicinity of electro-mechanical instabilities, and the latter is only applicable to oscillatory motion. A somewhat more promising approach to improve the performance of DE actuators is to design and fabricate *composite* materials with enhanced electro-mechanical coupling. Improvement in electro-mechanical coupling by orders of magnitude has been illustrated experimentally in DE composite materials (Huang and Zhang, 2004; Stoyanov et al., 2011). Moreover, theoretical studies on DE composites with periodic microstructures predict even more efficient performance (Goshkoderia et al., 2020; Rudykh et al., 2013; Tian et al., 2012). Furthermore, recent advances in the fabrication of microstructured materials at different length scales can further aid us in realizing this approach experimentally (Kolle et al., 2013; Lee and Fang, 2012; Li et al., 2018a; Zheng et al., 2014).

Although heterogeneities may allow us to access the enhanced electro-mechanical coupled behavior, they also make composite materials susceptible to instabilities. The instability phenomenon in composite materials subjected to purely mechanical loading has been studied extensively (Arora et al., 2019, 2020; Bertoldi and

* Corresponding author.
*E-mail address:* rudykh@wisc.edu (S. Rudykh).

https://doi.org/10.1016/j.euromechsol.2022.104534
Received 23 June 2021; Received in revised form 8 January 2022; Accepted 21 January 2022
Available online 25 January 2022

Lopez-Pamies, 2012; El Hamdaoui et al., 2015, 2020; Li et al., 2019, 2021; Merodio and Ogden, 2003, 2005a, 2005b, 2005c; Rudykh and deBotton, 2012; Slesarenko and Rudykh, 2017; Triantafyllidis and Maker, 1985; Triantafyllidis et al., 2006). Moreover, the stability and propagation of waves in the soft composites and structures are significantly influenced by the presence of residual stresses (Dehghani et al., 2019; Melnikov et al., 2021; Nam et al., 2016; Rodríguez and Merodio, 2016). Regarding DE composites, Bertoldi and Gei (2011), Rudykh and Debotton (2011), and Rudykh et al. (2014) analyzed electro-mechanical instabilities in soft layered DEs. Goshkoderia and Rudykh (2017) investigated the onset of macroscopic electro-mechanical instabilities in periodic DE composites with circular and elliptic inclusions. Recently, Polukhov et al. (2018) studied the onset of instabilities at different length-scales in DE composites with various microstructures. These studies illustrate the dependency of DE *material* stability on the applied electric field and pre-stretch, together with their microstructure.

On the structural level, DE plates are also prone to other failure modes such as dielectric breakdown, pull-in instability (Stark and Garton, 1955). The theoretical analysis allowed predicting these instabilities in the context of homogeneous deformation assumptions (Díaz-Calleja et al., 2009; Sharma et al., 2018; Xu et al., 2010; Zhao et al., 2007; Zhao and Suo, 2007; Zhu et al., 2010). However, in several experiments, it has been observed that the DE actuators undergo inhomogeneous deformation (Blok and LeGrand, 1969; Sharma et al., 2019); for instance, wrinkling appears before pull-in instability (Liu et al., 2016; Mao et al., 2021; Plante and Dubowsky, 2006). These experimental observations further motivated the theoretical developments in this direction. For example, De Tommasi et al. (2010) developed a simplified model to account for the non-homogeneous deformation states in thin electroelastic films. Later, De Tommasi et al. (2011) investigated the onset of wrinkling in thin-film DEs, by employing an approach based on tension field theory. By employing the theory of linearized incremental deformations and electric field (Dorfmann and Ogden, 2005, 2010), Dorfmann and Ogden (2014) investigated the diffuse mode of instabilities in a thin homogeneous neo-Hookean DE plate. Zurlo et al. (2017) analyzed the localized thinning phenomenon in one-side constrained and unconstrained DE films. Recently, Su et al. (2018) derived closed-form expressions corresponding to the onset of wrinkling phenomenon in DE plates by employing Stroh formulation. More recently, Zeng and Gao (2020) studied the effect of material anisotropy on the stability of a pre-stretched DE plate, by employing the linearized incremental theory. Furthermore, Broderick et al. (2020) performed the stability analysis of charge-controlled DE plates. Finally, we shall mention the work by Dorfmann and Ogden (2019), reviewing the theoretical analysis of the instabilities.

These various instability modes altogether pose several challenges in designing optimized devices based on DEs and thus require careful modeling and analysis. Moreover, the knowledge on electro-mechanical instabilities may provide additional tools to exploit the phenomenon to design microstructured materials with switchable functionalities (Babaee et al., 2016; Bertoldi and Boyce, 2008; Li et al., 2018b; Rudykh and Boyce, 2014). In the electro-mechanical instability analysis, the modeling of DE serves as a fundamental tool. The pioneering works by Toupin (1960) and (1956) laid the foundation for the non-linear electroelasticity theory, which has been reformulated and further developed (Dorfmann and Ogden, 2005, 2010; Liu, 2013; McMeeking and Landis, 2005; Suo et al., 2008; Zhao and Suo, 2010). Additionally, the convexity aspects of electro-elasticity energy functions have been investigated by Itskov and Khiêm (2016) and Ortigosa and Gil (2016). In parallel, significant efforts have been made in implementing the framework into the numerical schemes (Aboudi, 2015; Jabareen, 2015; Keip et al., 2014; Mehnert et al., 2019; Park et al., 2012; Sharma and Joglekar, 2019a, b; Vu et al., 2007).

In this paper, we investigate the interplay between the microstructure and stability of *composite* DE plates. In particular, we analyze the DE plates made out of layered material and determine the onset of their *structural* instability depending on the microstructural parameters (such as volume fractions and material properties of the phases). These results are compared with the predictions of *material* instabilities for the DE laminates. The paper is structured as follows. Sec. 2 summarizes the electroelasticity framework theoretical background. This is followed by the incremental constitutive equations and the incremental electric and mechanical boundary conditions presented in Sec. 3. In Sec. 4, the stability problem of the DE plates made out of isotropic incompressible constituents is analyzed. Sec. 5 illustrates the dependence of the onset of plate instabilities on microstructural parameters; the examples are shown with the comparison of the material instabilities.

## 2. Nonlinear theory of electroelasticity

Consider a deformable electroelastic material in the absence of volumetric free charges within the material. $\mathfrak{B}_r$ and $\mathfrak{B}$ indicate the initial and current configurations of the material respectively with boundaries $\partial\mathfrak{B}_r$ and $\partial\mathfrak{B}$. The general motion is described by the mapping $\boldsymbol{x} = \boldsymbol{f}(\boldsymbol{X},t)$, where $\boldsymbol{x}$ is the spatial position at time $t$ of a material particle with the material coordinate $\boldsymbol{X}$. The deformation gradient is $\boldsymbol{F} = \partial\boldsymbol{x}/\partial\boldsymbol{X}$. Then, the volume change of the body with respect to the reference configuration is defined by $J \equiv det\boldsymbol{F} > 0$.

We consider the quasi-electrostatic approximation, assuming that there are no electric fields nor free body charges and currents within the material. The electro-statics equations in the deformed state are

$$curl\, \boldsymbol{E} = \boldsymbol{0}, \qquad div\, \boldsymbol{D} = 0 \tag{1}$$

where $\boldsymbol{E}$ and $\boldsymbol{D}$ are the electric field and electric displacement vectors, respectively.

Considering the free surface charge per unit area of $\mathfrak{B}$ as $\sigma_f$, the electrostatic boundary conditions are as follows (Dorfmann and Ogden, 2014)

$$\boldsymbol{n} \times (\boldsymbol{E}^* - \boldsymbol{E}) = \boldsymbol{0}, \qquad \boldsymbol{n}\cdot(\boldsymbol{D}^* - \boldsymbol{D}) = \sigma_f \tag{2}$$

where $\boldsymbol{E}^*$ and $\boldsymbol{D}^*$ are the electric field and electric displacement in a vacuum surrounding $\mathfrak{B}$; $\boldsymbol{n}$ is the unit vector outward normal to the boundary $\partial\mathfrak{B}$.

The relations between Lagrangian and Eulerian electric field and electric displacement are defined as $\boldsymbol{E}^0 = \boldsymbol{F}^T\boldsymbol{E}$ and $\boldsymbol{D}^0 = J\boldsymbol{F}^{-1}\boldsymbol{D}$. Thus, the Lagrangian form of the boundary conditions reads as

$$\left(\boldsymbol{F}^T\boldsymbol{E}^* - \boldsymbol{E}^0\right) \times \boldsymbol{N} = \boldsymbol{0}, \qquad \left(J\boldsymbol{F}^{-1}\boldsymbol{D}^* - \boldsymbol{D}^0\right)\cdot\boldsymbol{N} = \sigma_F \tag{3}$$

where $\sigma_F$ denotes the free surface charge per unit area of $\mathfrak{B}_r$ and $\boldsymbol{N}$ is the unit outward normal to the boundary $\partial\mathfrak{B}_r$.

The equilibrium equation in the absence of mechanical body forces is

$$div\, \boldsymbol{\tau} = \boldsymbol{0} \tag{4}$$

where $\boldsymbol{\tau}$ is the *total* Cauchy stress tensor. The following traction boundary condition needs to be satisfied

$$\boldsymbol{\tau n} = \boldsymbol{t}_m + \boldsymbol{t}_e^*, \tag{5}$$

where $\boldsymbol{t}_m$ and $\boldsymbol{t}_e^*$ represent the mechanical and Maxwell traction vectors, respectively. The corresponding Maxwell stress tensor (in the vacuum) is

$$\boldsymbol{\tau}_e^* = \varepsilon_0\boldsymbol{E}^* \otimes \boldsymbol{E}^* - \frac{1}{2}\varepsilon_0(\boldsymbol{E}^*\cdot\boldsymbol{E}^*)\boldsymbol{I}, \tag{6}$$

where $\varepsilon_0$ denotes the vacuum permittivity, and $\boldsymbol{I}$ is the identity tensor.

The total first Piola-Kirchhoff stress tensor $\boldsymbol{P}$ is related to the total Cauchy stress via $\boldsymbol{P} = J\boldsymbol{\tau}\boldsymbol{F}^{-T}$. The referential form of the equilibrium equation is

$$Div\, \boldsymbol{P} = \boldsymbol{0} \tag{7}$$

The corresponding traction boundary condition (5) transforms to

$$\boldsymbol{PN} = \boldsymbol{t}_M + \boldsymbol{t}_E^* \tag{8}$$

where $\boldsymbol{t}_M$ is the mechanical traction per unit area of $\partial\mathfrak{B}_r$ and $\boldsymbol{t}_E^* = \boldsymbol{P}_E^*\boldsymbol{N}$ with $\boldsymbol{P}_E^* = J\boldsymbol{\tau}_e^*\boldsymbol{F}^{-T}$.

For an electroelastic incompressible material, the first Piola-Kirchhoff stress tensor and Lagrangian electric field can be defined through a scalar-valued energy-density function $w(\boldsymbol{F}, \boldsymbol{D}^0)$, namely,

$$\boldsymbol{P} = \frac{\partial w(\boldsymbol{F}, \boldsymbol{D}^0)}{\partial \boldsymbol{F}} - q\boldsymbol{F}^{-T}, \qquad \boldsymbol{E}^0 = \frac{\partial w(\boldsymbol{F}, \boldsymbol{D}^0)}{\partial \boldsymbol{D}^0} \tag{9}$$

Here, $q$ is the Lagrange multiplier arising from the incompressibility constraint. Consequently, the total Cauchy stress and current electric field are given by

$$\boldsymbol{\tau} = \frac{\partial w(\boldsymbol{F}, \boldsymbol{D}^0)}{\partial \boldsymbol{F}}\boldsymbol{F}^T - q\boldsymbol{I}, \qquad \boldsymbol{E} = \boldsymbol{F}^{-T}\frac{\partial w(\boldsymbol{F}, \boldsymbol{D}^0)}{\partial \boldsymbol{D}^0} \tag{10}$$

## 3. Incremental equations and boundary conditions

In this section, the framework of the incremental deformations superimposed on a finitely deformed configuration is summarized based on the work by Dorfmann and Ogden (2014). The framework will be further applied to investigate the instability of a composite dielectric plate subject to an in-plane equibiaxial stretch under the action of an electric field applied through the thickness of the plate.

Let us denote the increments in the Lagrangian electric field, electric displacement, and the first Piola-Kirchhoff stress tensor by $\dot{\boldsymbol{E}}^0$, $\dot{\boldsymbol{D}}^0$ and $\dot{\boldsymbol{P}}$, respectively. The corresponding incremental governing equations are

$$Curl\,\dot{\boldsymbol{E}}^0 = \boldsymbol{0}, \qquad Div\,\dot{\boldsymbol{D}}^0 = 0, \qquad Div\,\dot{\boldsymbol{P}} = \boldsymbol{0} \tag{11}$$

Consequently, the incremental form of the electrical and traction boundary conditions can be written as

$$\begin{aligned} &\left(\dot{\boldsymbol{F}}^T\boldsymbol{E}^* + \boldsymbol{F}^T\dot{\boldsymbol{E}}^* - \dot{\boldsymbol{E}}^0\right) \times \boldsymbol{N} = \boldsymbol{0} && on\ \partial\mathfrak{B}_r \\ &\left(\boldsymbol{F}^{-1}\dot{\boldsymbol{D}}^* - \boldsymbol{F}^{-1}\dot{\boldsymbol{F}}\boldsymbol{F}^{-1}\boldsymbol{D}^* - \dot{\boldsymbol{D}}^0\right)\cdot\boldsymbol{N} = 0 && on\ \partial\mathfrak{B}_r \\ &\dot{\boldsymbol{P}}\boldsymbol{N} = \dot{\boldsymbol{t}}_M + \dot{\boldsymbol{\tau}}_e^*\boldsymbol{F}^{-T}\boldsymbol{N} - \boldsymbol{\tau}_e^*\boldsymbol{F}^{-T}\dot{\boldsymbol{F}}^T\boldsymbol{F}^{-T}\boldsymbol{N} && on\ \partial\mathfrak{B}_r \end{aligned} \tag{12}$$

Here, $\dot{\boldsymbol{E}}^*$ and $\dot{\boldsymbol{D}}^*$ are the increments of the electric field and electric displacement outside the material; these satisfy the equations $curl\,\dot{\boldsymbol{E}}^* = \boldsymbol{0}$, $div\,\dot{\boldsymbol{D}}^* = 0$; the increment in the Maxwell stress tensor $\dot{\boldsymbol{\tau}}_e^*$ is expressed as

$$\dot{\boldsymbol{\tau}}_e^* = \varepsilon_0[\dot{\boldsymbol{E}}^* \otimes \boldsymbol{E}^* + \boldsymbol{E}^* \otimes \dot{\boldsymbol{E}}^* - (\boldsymbol{E}^*\cdot\dot{\boldsymbol{E}}^*)\boldsymbol{I}] \tag{13}$$

In the following, the "push-forward" transformation of the variables – denoted by a superscript "∧" – is employed, in particular,

$$\widehat{\boldsymbol{E}} = \boldsymbol{F}^{-T}\dot{\boldsymbol{E}}^0, \qquad \widehat{\boldsymbol{D}} = \boldsymbol{F}\dot{\boldsymbol{D}}^0, \qquad \widehat{\boldsymbol{P}} = \dot{\boldsymbol{P}}\boldsymbol{F}^T \tag{14}$$

The incremental Eq. (11) transform into

$$curl\,\widehat{\boldsymbol{E}} = \boldsymbol{0}, \qquad div\,\widehat{\boldsymbol{D}} = 0, \qquad div\,\widehat{\boldsymbol{P}} = \boldsymbol{0} \tag{15}$$

and the corresponding boundary conditions are

$$\begin{aligned} &\left(\dot{\boldsymbol{E}}^* + \boldsymbol{L}^T\boldsymbol{E}^* - \widehat{\boldsymbol{E}}\right) \times \boldsymbol{n} = \boldsymbol{0} && on\partial\mathfrak{B} \\ &\left(\dot{\boldsymbol{D}}^* - \boldsymbol{L}\boldsymbol{D}^* - \widehat{\boldsymbol{D}}\right)\cdot\boldsymbol{n} = 0 && on\partial\mathfrak{B} \\ &\widehat{\boldsymbol{P}}\boldsymbol{n} = \widehat{\boldsymbol{t}}_M + \dot{\boldsymbol{\tau}}_e^*\boldsymbol{n} - \boldsymbol{\tau}_e^*\boldsymbol{L}^T\boldsymbol{n} && on\partial\mathfrak{B} \end{aligned} \tag{16}$$

The linearized constitutive laws for an incompressible material are

$$\dot{\boldsymbol{P}} = \mathcal{A}^0\dot{\boldsymbol{F}} + \mathcal{B}^0\dot{\boldsymbol{D}}^0 - \dot{q}\boldsymbol{F}^{-T} + q\boldsymbol{F}^{-T}\dot{\boldsymbol{F}}^T\boldsymbol{F}^{-T}$$

$$\dot{\boldsymbol{E}}^0 = \mathcal{B}^{0T}\dot{\boldsymbol{F}} + \mathcal{C}^0\dot{\boldsymbol{D}}^0 \tag{17}$$

in which $\mathcal{A}^0$, $\mathcal{B}^0$, $\mathcal{C}^0$ stand for the electroelastic moduli tensors associated with the energy function $w(\boldsymbol{F}, \boldsymbol{D}^0)$. In particular, the tensors of the electroelastic moduli are defined as

$$\mathscr{A}^0_{\alpha j\beta l} = \frac{\partial^2 w}{\partial F_{\alpha j}\partial F_{\beta l}}, \qquad \mathscr{B}^0_{i\alpha\beta} = \frac{\partial^2 w}{\partial F_{i\alpha}\partial D^0_\beta}, \qquad \mathscr{C}^0_{\alpha\beta} = \frac{\partial^2 w}{\partial D^0_\alpha \partial D^0_\beta} \tag{18}$$

The updated forms of Eqs. (17) are

$$\widehat{\boldsymbol{P}} = \mathcal{A}\boldsymbol{L} + \mathcal{B}\widehat{\boldsymbol{D}} + q\boldsymbol{L}^T - \dot{q}\boldsymbol{I}$$

$$\widehat{\boldsymbol{E}} = \mathcal{B}^T\boldsymbol{L} + \mathcal{C}\widehat{\boldsymbol{D}} \tag{19}$$

The updated tensors of the electroelastic moduli are related to $\mathcal{A}^0$, $\mathcal{B}^0$ and $\mathcal{C}^0$ via

$$\mathscr{A}_{ijkl} = J^{-1}F_{j\alpha}F_{l\beta}\mathscr{A}^0_{i\alpha k\beta}, \qquad \mathscr{B}_{ijk} = F_{j\alpha}F^{-1}_{\beta k}\mathscr{B}^0_{i\alpha\beta}, \qquad \mathscr{C}_{ij} = JF^{-1}_{\alpha i}F^{-1}_{\beta j}\mathscr{C}^0_{\alpha\beta} \tag{20}$$

with the symmetries

$$\mathscr{A}_{ijkl} = \mathscr{A}_{klij}, \qquad \mathscr{B}_{ijk} = \mathscr{B}_{jik}, \qquad \mathscr{C}_{ij} = \mathscr{C}_{ji} \tag{21}$$

## 4. Application to layered dielectric elastomer plates

Consider a composite electroelastic plate made out of two isotropic incompressible constituents with volume fractions $c^{(f)}$ and $c^{(m)} = 1 - c^{(f)}$. The plate is covered by flexible electrodes on its major surfaces and subjected to planar biaxial deformation under the action of an electric field applied through the plate thickness as illustrated in Fig. 1.

The reference geometry of the plate is defined as

$$-L_1 \le X_1 \le L_1, \quad -\frac{H}{2} \le X_2 \le \frac{H}{2}, \quad -L_3 \le X_3 \le L_3 \tag{22}$$

where $H$ is the initial thickness of the plate. Here $X_1, X_2, X_3$ represent a material point in the undeformed configuration and $x_1, x_2, x_3$ represent its position in the deformed configuration. The plate is subjected to planar equi-biaxial stretch $\lambda_1 = \lambda_3 = \lambda$ and to an electric displacement with components $D_2 = D^0, D_1 = D_3 = 0$. For incompressibility of the material $\lambda_2 = \lambda^{-2}$. Thus, the average deformation gradient $\overline{\boldsymbol{F}}$ and average electric displacement $\overline{\boldsymbol{D}}^0$ can be written as

$$\overline{\boldsymbol{F}} = \lambda(\boldsymbol{I} - \boldsymbol{e}_2 \otimes \boldsymbol{e}_2) + \lambda^{-2}\boldsymbol{e}_2 \otimes \boldsymbol{e}_2, \quad \overline{\boldsymbol{D}}^0 = \overline{D}^0\boldsymbol{e}_2 \tag{23}$$

$\lambda$ is the average stretch ratio in the direction of the layers; the average stretch ratio is defined as $\lambda = \lambda^{(f)}c_f + \lambda^{(m)}c_m$.

Next, we consider the superimposed incremental displacement field $\boldsymbol{u}$, the incompressibility condition under the plane-strain condition imposes that $u_{1,1} + u_{2,2} = 0$. Thus, there exists a function $\psi = \psi(x_1, x_2)$ such that $u_1 = \psi_{,2}$ and $u_2 = -\psi_{,1}$. In a similar manner, assuming that the out of plane component of the electric displacement is zero in Eq. (15)$_2$, one can conclude that there exists a function $\varphi$ such that $\widehat{D}_1 = \varphi_{,2}$ and $\widehat{D}_2 = -\varphi_{,1}$. Thus, the updated incremental Eqs. (15)$_1$ and (15)$_3$ can be written in terms of the potential functions, namely,

$$\begin{aligned} &a\psi_{,1111} + 2b\psi_{,1122} + c\psi_{,2222} + (e-d)\varphi_{,112} + d\varphi_{,222} = 0 \\ &d\psi_{,222} + (e-d)\psi_{,112} + f\varphi_{,22} + g\varphi_{,11} = 0 \end{aligned} \tag{24}$$

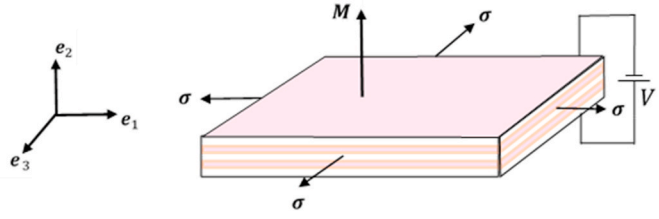


**Fig. 1.** Schematic of an anisotropic dielectric plate with the loading conditions.

Here, the material coefficients are

$$a=\mathscr{A}_{2121},\quad 2b=\mathscr{A}_{1111}+\mathscr{A}_{2222}-2\mathscr{A}_{1221},\quad c=\mathscr{A}_{1212},\\ d=\mathscr{B}_{211},\quad e=\mathscr{B}_{222},\quad f=\mathscr{C}_{11},\quad g=\mathscr{C}_{22} \tag{25}$$

From the plane-strain assumption in the $(x_1,x_2)$ plane, it can be deduced that a scalar function $\varphi^*(x_1,x_2)$ exists such that $\dot{E}_1^*=-\varphi_{,1}^*$ and $\dot{E}_2^*=-\varphi_{,2}^*$, where $\varphi^*$ satisfies Laplace's equation. Setting the incremental mechanical traction to zero, the incremental traction and electrical boundary conditions (16) in terms of $\psi$ and $\varphi$ take the following form

$$\begin{aligned}
&(\tau_{22}+\tau_{e22}^*-c)\psi_{,11}+c\psi_{,22}+d\varphi_{,2}+D_2^*\varphi_{,1}^*=0 \quad on \quad x_2=\pm\frac{h}{2}\\
&(2b+c-\tau_{22}+\tau_{e22}^*)\psi_{,112}+c\psi_{,222}+e\varphi_{,11}+d\varphi_{,22}-D_2^*\varphi_{,12}^*=0 \quad on \quad x_2=\pm\frac{h}{2}\\
&(\varepsilon_0^{-1}D_2^*-d)\psi_{,11}+d\psi_{,22}+f\varphi_{,2}+\varphi_{,1}^*=0 \quad on \quad x_2=\pm\frac{h}{2}\\
&\varphi_{,1}-\varepsilon_0\varphi_{,2}^*+D_2^*\psi_{,12}=\dot{\sigma}_{F0} \quad on \quad x_2=\pm\frac{h}{2}
\end{aligned} \tag{26}$$

Here $h=\lambda^{-2}H$ denotes the deformed plate thickness. On the boundaries $x_2=\pm\frac{h}{2}$, it can be prescribed either the electrostatic potential or the charge density. We will use the first option so that the incremental boundary conditions specialize to $\widehat{E}_1=0$, and $(26)_3$ applies. In the absence of the mechanical traction on the faces $x_2=\pm\frac{h}{2}$, the total stress component $\tau_{22}=0$. Here, we consider the case when the top and bottom surfaces of the dielectric plate are coated by flexible electrodes. Thus, there is no external field, and as a result Eqs. (26) reduce to

$$\begin{aligned}
&(\psi_{,22}-\psi_{,11})=0 \quad on \quad x_2=\pm\frac{h}{2}\\
&(2b+c)\psi_{,112}+c\psi_{,222}+e\varphi_{,11}+d\varphi_{,22}=0 \quad on \quad x_2=\pm\frac{h}{2}\\
&\varphi_{,2}=0 \quad on \quad x_2=\pm\frac{h}{2}
\end{aligned} \tag{27}$$

We seek a solution for the incremental boundary-value problem in the following form (Dorfmann and Ogden, 2014)

$$\psi=Ae^{-ksx_2}e^{ikx_1},\qquad \varphi=kBe^{-ksx_2}e^{ikx_1} \tag{28}$$

where $k$ is the wavenumber of the perturbation, and $s$ is a parameter to be obtained. Substitution of these functions into Eq. (24) and setting the determinant of the coefficients matrix equal to zero leads to an equation from which one can determine $s$

$$(cf-d^2)s^6-[2bf+cg+2(d-e)d]s^4+\left[2bg+af-(d-e)^2\right]s^2-ag=0 \tag{29}$$

It is easy to see that this equation is cubic in $t=s^2$. The roots are denoted by $s_1,s_2,s_3,s_4=-s_1,s_5=-s_2,s_6=-s_3$. Substitution of the general solution $\psi=\sum_{j=1}^6 A_je^{-ks_jx_2}e^{ikx_1}$ and $\varphi=\sum_{j=1}^6 kB_je^{-ks_jx_2}e^{ikx_1}$ into the boundary conditions (27) yields

$$\sum_{j=1}^6\alpha_je_j^{\pm}B_j=0,\qquad \sum_{j=1}^6\beta_je_j^{\pm}B_j=0,\qquad \sum_{j=1}^6\gamma_je_j^{\pm}B_j=0,\qquad on\quad x_2=\pm\frac{h}{2} \tag{30}$$

where $e_j^{\pm}=e^{\pm\frac{ks_jh}{2}}$. Using the relation between $A_j$ and $B_j$ (Dorfmann and Ogden, 2014), the coefficients $\alpha_j,\beta_j$ and $\gamma_j$ can be written as

$$\begin{aligned}
&\alpha_j=\frac{s_j\left(1+s_j^2\right)\left(ds_j^2+d-e\right)}{cs_j^4-2bs_j^2+a},\\
&\beta_j=\frac{[(2b+c+a)d-ce]s_j^2-ae}{cs_j^4-2bs_j^2+a},\\
&\gamma_j=s_j
\end{aligned} \tag{31}$$

Next, we specify the analysis for DE laminate plate (see Fig. 1) with isotropic incompressible dielectric phases characterized by the neo-Hookean ideal dielectric model

$$w^{(r)}=\frac{\mu^{(r)}}{2}\left(\boldsymbol{F}^{(r)}:\boldsymbol{F}^{(r)}-3\right)+\frac{1}{2\varepsilon^{(r)}}\boldsymbol{D}^{0(r)}\cdot\boldsymbol{C}^{(r)}\dot{c}\boldsymbol{D}^{0(r)} \tag{32}$$

where $\mu^{(r)}$ and $\varepsilon^{(r)}$ respectively denote the shear moduli and dielectric constants of the two phases; $\boldsymbol{C}^{(r)}$ is the right Cauchy-Green deformation tensor.

For this case, it has been shown that an explicit exact solution can be obtained for the local fields in the laminate phases (see (Galich and Rudykh, 2017; Rudykh et al., 2014; Rudykh and Debotton, 2011; Spinelli and Lopez-Pamies, 2015)). Moreover, based on the exact solution, the effective energy function can be constructed, namely,

$$w(\overline{\boldsymbol{F}},\overline{\boldsymbol{D}}^0)=\frac{\overline{\mu}}{2}(\overline{\boldsymbol{F}}:\overline{\boldsymbol{F}}-3)-\frac{\overline{\mu}-\breve{\mu}}{2}\left(\boldsymbol{M}\cdot\overline{\boldsymbol{C}}\boldsymbol{M}-\frac{1}{\boldsymbol{M}\cdot\overline{\boldsymbol{C}}^{-1}\boldsymbol{M}}\right)+\frac{1}{2\overline{\varepsilon}}\overline{\boldsymbol{D}}^0\cdot\overline{\boldsymbol{C}}\overline{\boldsymbol{D}}^0+\frac{1}{2}\left(\frac{1}{\breve{\varepsilon}}-\frac{1}{\overline{\varepsilon}}\right)\frac{(\overline{\boldsymbol{D}}^0\cdot\boldsymbol{M})^2}{\boldsymbol{M}\cdot\overline{\boldsymbol{C}}^{-1}\boldsymbol{M}} \tag{33}$$

where $\overline{\boldsymbol{F}}$ and $\overline{\boldsymbol{D}}^0$ are the average deformation gradient and electric displacement, respectively; $\boldsymbol{M}$ denotes the initial lamination direction; the effective arithmetic and harmonic averages of the material constants are

$$\begin{aligned}
&\overline{\mu}=c^{(f)}\mu^{(f)}+c^{(m)}\mu^{(m)},\quad \breve{\mu}=\left(\frac{c^{(f)}}{\mu^{(f)}}+\frac{c^{(m)}}{\mu^{(m)}}\right)^{-1}\\
&\overline{\varepsilon}=c^{(f)}\varepsilon^{(f)}+c^{(m)}\varepsilon^{(m)},\quad \breve{\varepsilon}=\left(\frac{c^{(f)}}{\varepsilon^{(f)}}+\frac{c^{(m)}}{\varepsilon^{(m)}}\right)^{-1}
\end{aligned} \tag{34}$$

We note that the effective energy function is derived based on the exact solution for the finitely deformed dielectric laminates. By applying the loss of ellipticity condition, the critical deformation and applied field corresponding to the onset of macroscopic instability can be determined. Specifically, for the average deformation gradient (23), introducing the incremental equation (19) into the electrostatic equation (15) along with the incompressibility condition gives the critical stretch $\lambda_{cr}^m$ and critical electric displacement $\overline{D}_{cr}^0$ as follows (Galich and Rudykh, 2017)

$$\begin{aligned}
&\lambda_{cr}^m=\left(\frac{\overline{D}_{cr}^{(0)\,2}}{\overline{\mu}\overline{\varepsilon}}\left(1-\frac{\breve{\varepsilon}}{\overline{\varepsilon}}\right)-\frac{\breve{\mu}}{\overline{\mu}}+1\right)^{1/6}\\
&\frac{\overline{D}_{cr}^0}{\sqrt{\overline{\mu}\overline{\varepsilon}}}=\left(\lambda_{cr}^{(m)\,6}+\frac{\breve{\mu}}{\overline{\mu}}-1\right)^{1/2}\left(1-\frac{\breve{\varepsilon}}{\overline{\varepsilon}}\right)^{-1/2}
\end{aligned} \tag{35}$$

We refer to the macroscopic instability criterion as the *material* instability (Bertoldi and Gei, 2011); in the sequel, we compare condition (35) with the structural instability analysis of the plate made out of the composite material described by the effective energy function given in

Eq. (33).

By making use of the energy function (33), the tensors of the electroelastic moduli defined in Eq. (20) are determined, thus, allowing us to derive the explicit expressions for the material coefficients defined in Eq. (25), namely,

$$
\begin{aligned}
&a = \lambda^{-4}\left[\overline{\mu}\left(\lambda^6-1\right)+\breve{\mu}+\overline{D}^{0\,2}\left(\frac{1}{\overline{\varepsilon}}-\frac{1}{\breve{\varepsilon}}\right)\right]\\
&2b = \lambda^{-4}\left[\overline{\mu}\left(\lambda^6+3\right)-2\breve{\mu}+\overline{D}^{0\,2}\left(\frac{3}{\breve{\varepsilon}}-\frac{2}{\overline{\varepsilon}}\right)\right],\quad c = \lambda^{-4}\left[\breve{\mu}+\frac{\overline{D}^{0\,2}}{\overline{\varepsilon}}\right],\\
&d = \frac{\overline{D}^0}{\lambda^2\overline{\varepsilon}},\quad e = \frac{2\overline{D}^0}{\lambda^2\breve{\varepsilon}},\quad f = \frac{1}{\overline{\varepsilon}},\quad g = \frac{1}{\breve{\varepsilon}}
\end{aligned}
\tag{36}
$$

Using the microscopic electroelastic moduli (36), the coefficients (31) take the following form

$$
\begin{aligned}
\alpha_j &= \frac{s_j\left(1+s_j^2\right)\lambda^2\dfrac{\overline{D}}{\sqrt{\overline{\mu}\breve{\varepsilon}}}\left(s_j^2-2\,\dfrac{\overline{\varepsilon}}{\breve{\varepsilon}}+1\right)}{\left(\overline{D}^2+\dfrac{\overline{\varepsilon}}{\breve{\varepsilon}}\right)s_j^4-\left[\dfrac{\overline{\mu}}{\breve{\mu}}\,\dfrac{\overline{\varepsilon}}{\breve{\varepsilon}}\left(\lambda^6+3\right)-2\,\dfrac{\overline{\varepsilon}}{\breve{\varepsilon}}+\overline{D}^2\left(3\,\dfrac{\overline{\varepsilon}}{\breve{\varepsilon}}-2\right)\right]s_j^2+\dfrac{\overline{\mu}}{\breve{\mu}}\,\dfrac{\overline{\varepsilon}}{\breve{\varepsilon}}\left(\lambda^6-1\right)+\overline{D}^2\left(1-\dfrac{\overline{\varepsilon}}{\breve{\varepsilon}}\right)+\dfrac{\overline{\varepsilon}}{\breve{\varepsilon}}}\\
\beta_j &= \frac{\dfrac{2\overline{D}}{\lambda^2}\sqrt{\dfrac{\breve{\mu}}{\breve{\varepsilon}}}\left\{\left[\dfrac{\overline{\mu}}{\breve{\mu}}\left(\lambda^6+1\right)-\dfrac{\overline{\varepsilon}}{\breve{\varepsilon}}\right]s_j^2-\dfrac{\overline{\mu}}{\breve{\mu}}\,\dfrac{\overline{\varepsilon}}{\breve{\varepsilon}}\left(\lambda^6-1\right)-\overline{D}^2\left(1-\dfrac{\overline{\varepsilon}}{\breve{\varepsilon}}\right)-\dfrac{\overline{\varepsilon}}{\breve{\varepsilon}}\right\}}{\left(\overline{D}^2+\dfrac{\overline{\varepsilon}}{\breve{\varepsilon}}\right)s_j^4-\left[\dfrac{\overline{\mu}}{\breve{\mu}}\,\dfrac{\overline{\varepsilon}}{\breve{\varepsilon}}\left(\lambda^6+3\right)-2\,\dfrac{\overline{\varepsilon}}{\breve{\varepsilon}}+\overline{D}^2\left(3\,\dfrac{\overline{\varepsilon}}{\breve{\varepsilon}}-2\right)\right]s_j^2+\dfrac{\overline{\mu}}{\breve{\mu}}\,\dfrac{\overline{\varepsilon}}{\breve{\varepsilon}}\left(\lambda^6-1\right)+\overline{D}^2\left(1-\dfrac{\overline{\varepsilon}}{\breve{\varepsilon}}\right)+\dfrac{\overline{\varepsilon}}{\breve{\varepsilon}}}\\
\gamma_j &= s_j
\end{aligned}
\tag{37}
$$

where $\overline{D} = \overline{D}^0/\sqrt{\overline{\mu}\breve{\varepsilon}}$ is dimensionless Lagrangian electric displacement perpendicular to the layers.

The analytical explicit formulas for roots $s_j$ with respect to the energy function (33) are given in Appendix A. It is clear from relations (37) that

$$
\alpha_{3+j} = -\alpha_j,\qquad \beta_{3+j} = \beta_j,\qquad \gamma_{3+j} = -\gamma_j \tag{38}
$$

Substitution of the coefficients (37) into the boundary conditions (30) yields a system of $6\times 6$ linear equations. Putting the determinant of the coefficients matrix equal to zero, we can obtain the bifurcation equations and determine the onset of instability

$$
det\begin{bmatrix}
\alpha_1e_1^- & \alpha_2e_2^- & \alpha_3e_3^- & -\alpha_1e_1^+ & -\alpha_2e_2^+ & -\alpha_3e_3^+\\
\beta_1e_1^- & \beta_2e_2^- & \beta_3e_3^- & \beta_1e_1^+ & \beta_2e_2^+ & \beta_3e_3^+\\
\gamma_1e_1^- & \gamma_2e_2^- & \gamma_3e_3^- & -\gamma_1e_1^+ & -\gamma_2e_2^+ & -\gamma_3e_3^+\\
\alpha_1e_1^+ & \alpha_2e_2^+ & \alpha_3e_3^+ & -\alpha_1e_1^- & -\alpha_2e_2^- & -\alpha_3e_3^-\\
\beta_1e_1^+ & \beta_2e_2^+ & \beta_3e_3^+ & \beta_1e_1^- & \beta_2e_2^- & \beta_3e_3^-\\
\gamma_1e_1^+ & \gamma_2e_2^+ & \gamma_3e_3^+ & -\gamma_1e_1^- & -\gamma_2e_2^- & -\gamma_3e_3^-
\end{bmatrix} = 0 \tag{39}
$$

The determinant can be factorized into two independent equations as

$$
\beta_1(\alpha_3\gamma_2-\alpha_2\gamma_3)T_1+\beta_2(\alpha_1\gamma_3-\alpha_3\gamma_1)T_2+\beta_3(\alpha_2\gamma_1-\alpha_1\gamma_2)T_3 = 0 \tag{40}
$$

$$
\frac{\beta_1(\alpha_3\gamma_2-\alpha_2\gamma_3)}{T_1}+\frac{\beta_2(\alpha_1\gamma_3-\alpha_3\gamma_1)}{T_2}+\frac{\beta_3(\alpha_2\gamma_1-\alpha_1\gamma_2)}{T_3} = 0
$$

in which $T_j = tanh(ks_jh/2)$.

The first equation represents the bifurcation equation for antisymmetric modes, and the second one corresponds to symmetric ones. The schematic illustrations of the antisymmetric and symmetric modes of wrinkling are depicted in Fig. 2.

Each of these bifurcation equations provides an implicit relation between the critical stretch $\lambda_{cr}^p$, applied electric field, normalized wavenumber, and material parameters. In the next section, some numerical examples are provided to illustrate the effect of different variables on the instabilities of composite DE plates.

## 5. Results and discussion

In this section, we illustrate the results of the plate instability analysis. The critical stretch and applied electric field corresponding to the antisymmetric and symmetric instability modes are determined by solving Eq. (40). The results for the electroelastic plate instabilities are further compared to the material instability results from Eq. (35) for the identical energy function (33). The comparison allows us to map both material and structural instabilities in the same dielectric composite design space and electro-mechanical loadings.

Fig. 3 shows the critical stretch as a function of the normalized wavenumber $kH$. The results are shown for the DE laminate plate with $c^{(f)} = 0.2$, $\chi = \mu^{(f)}/\mu^{(m)} = 10$ and $\xi = \varepsilon^{(f)}/\varepsilon^{(m)} = 10$; the DE laminate plate is subjected to different values of dimensionless electric displacement $\overline{D} = \overline{D}^0/\sqrt{\overline{\mu}\breve{\varepsilon}}$; namely, $\overline{D} = 0$, 1, 2, 2.63, 3, 4. The blue and red curves correspond to the antisymmetric and symmetric modes, respectively.

In each figure, the upper curve separates the stable domain from that in which instabilities may develop, i.e., the unstable region is enclosed by the area under the upper curve. The unstable domain increases as the applied electric displacement increases. This observation indicates that the electric field has a destabilizing effect in this configuration. Plots (a)-(f) show as the normalized wavenumber increases, the range of unstable stretch values reduces. Fig. 3(a) displays the results for the purely

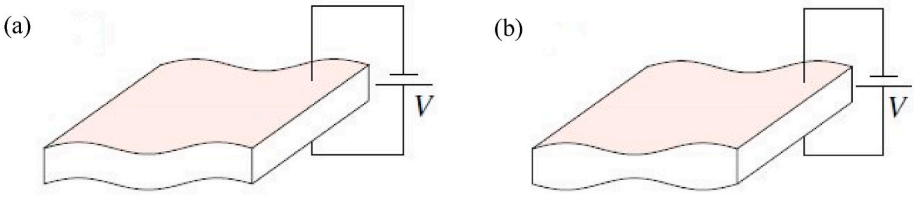


**Fig. 2.** Schematics for DE plate in (a) antisymmetric and (b) symmetric modes of instability.

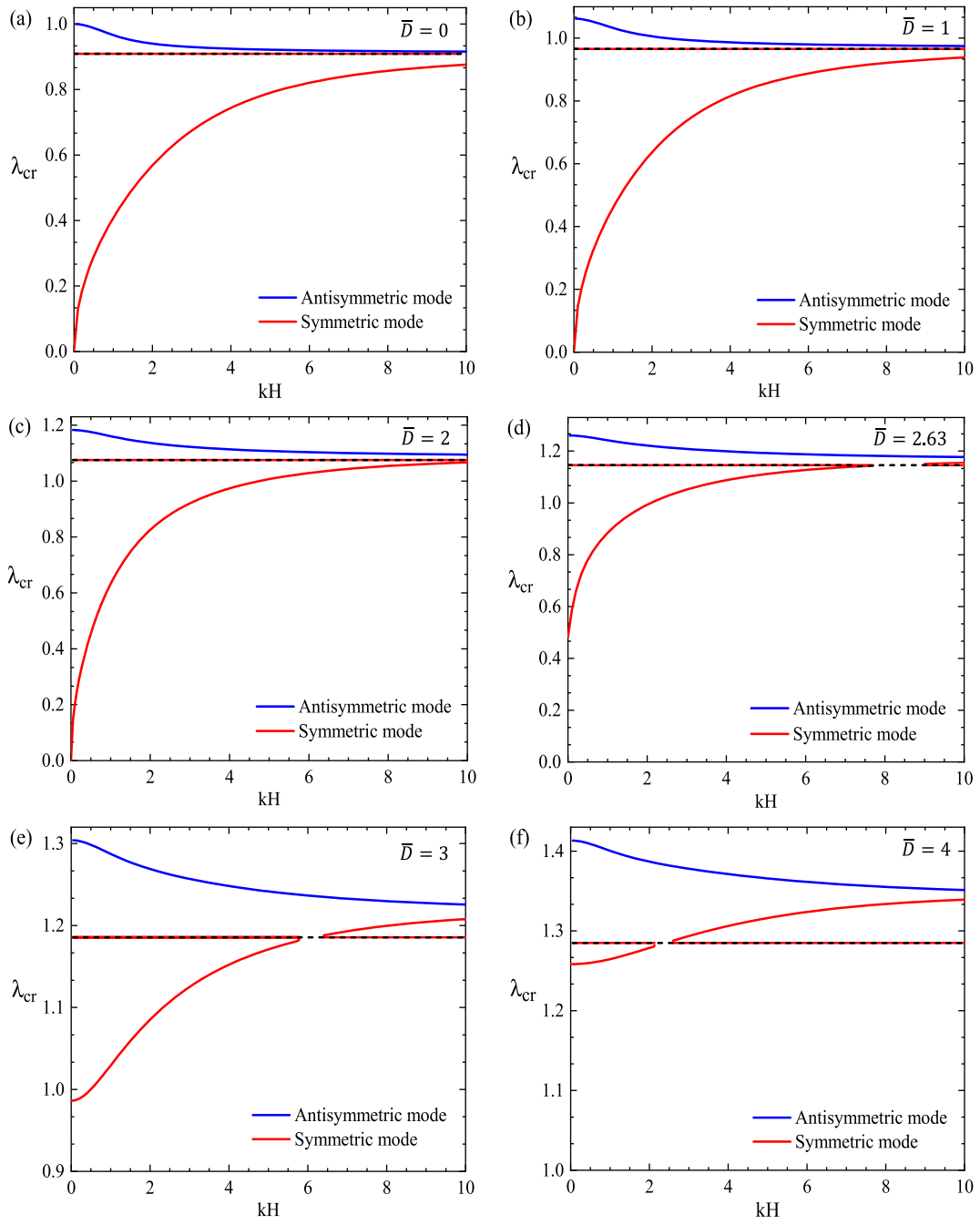


**Fig. 3.** The critical stretch versus the normalized wavenumber ($kH$) for the DE laminate plate with $c^{(f)} = 0.2, \chi = 10, \xi = 10$. The plate is subjected to different levels of electric excitation: $\overline{D} = 0$ (a), 1 (b), 2 (c), 2.63 (d), 3 (e), 4 (f). The blue and red curves denote the antisymmetric and symmetric bifurcation modes, respectively. (For interpretation of the references to colour in this figure legend, the reader is referred to the Web version of this article.)

mechanical case in the absence of an electric field. The blue curve corresponds to a flexural (antisymmetric) mode, while the red curve denotes the symmetric mode. As expected, for this purely elastic case, the antisymmetric mode occurs under compression of the plate, and develops first at $kH \to 0$. For the electrically excited cases ($\overline{D} > 0$), the plate is unstable even in the undeformed state $\lambda = 1$, and a pre-stretch (of the level depending on the applied electric field) is needed to reach the stable state and avoid the instability development. We note that at a certain level of the electric field, the symmetric bifurcation curve experiences a significant shape change; in particular, two distinct curves corresponding to the symmetric instability modes appear (instead of a single curve for the cases with lower levels of the applied electric field). This is illustrated by the example of the plate subjected to the electric excitation level $\overline{D} = 2.63$ in Fig. 3(d). The dotted horizontal lines coincide with the critical stretches corresponding to the macroscopic material instabilities (Galich and Rudykh, 2017; Goshkoderia and Rudykh, 2017; Rudykh et al., 2013, 2014; Rudykh and Debotton, 2011, 2012; Slesarenko and Rudykh, 2017).

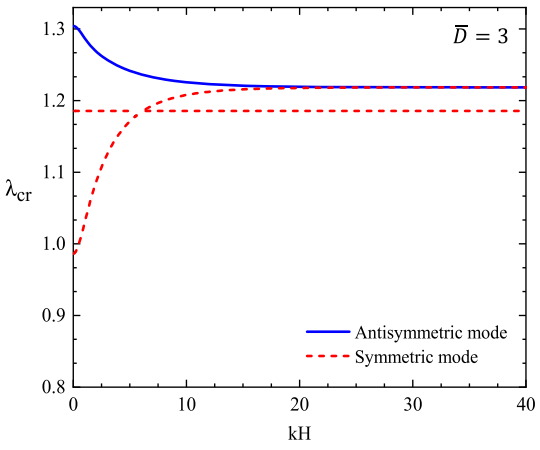


**Fig. 4.** The critical stretch versus the normalized wavenumber ($kH$) for the DE laminate plate with $c^{(f)} = 0.2$, $\chi = 10$, $\xi = 10$. The plate is subjected to the electric excitation $\overline{D} = 3$. The blue and red curves denote the antisymmetric and symmetric bifurcation modes, respectively. (For interpretation of the references to colour in this figure legend, the reader is referred to the Web version of this article.)

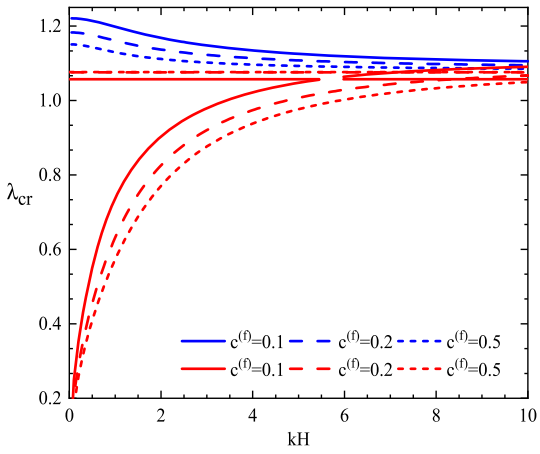


**Fig. 6.** The critical stretch versus the normalized wavenumber $kH$ for the DE laminate plate with $\chi = 10$, $\xi = 10$ and different volume fractions $c^{(f)} = 0.1$, 0.2, 0.5. The plate is subjected to electric excitation $\overline{D} = 2$. The blue and red curves denote the antisymmetric and symmetric modes, respectively. (For interpretation of the references to colour in this figure legend, the reader is referred to the Web version of this article.)

Note that the antisymmetric and symmetric mode curves approach each other as the wavenumber is increased. Fig. 4 displays the dependence of the critical stretch on the normalized wavenumber $kH$ for a wide range to illustrate the asymptotic behavior of the mode curves. The example is given for the composite with $c^{(f)} = 0.2, \chi = 10$, and $\xi = 10$, subjected to the electric excitation of $\overline{D} = 3$. The blue and red curves correspond to the antisymmetric and symmetric modes, respectively. The critical stretch curve for the antisymmetric instabilities decreases monotonically with an increase in $kH$, and then asymptotically approaches the level of $\lambda_{cr} \approx 1.22$. An opposite effect is observed for the symmetric bifurcation curve. The symmetric instability curve increases monotonically with $kH$, and then asymptotically approaches the values of $\lambda_{cr} \approx 1.22$.

For completeness, we also show the results for an isotropic neo-Hookean ideal dielectric plate in Fig. 5. The verification results are calculated for the composite dielectric plate with $c^{(f)} = 1$, $c^{(m)} = 0$, $(\mu^{(f)}/\mu^{(m)} = 1; \varepsilon^{(f)}/\varepsilon^{(m)} = 1)$; for this case, the effective energy function (33) reduces to that for isotropic media

$$w(\boldsymbol{F}, \boldsymbol{D}^0) = \frac{\mu}{2}(\boldsymbol{F} : \boldsymbol{F} - 3) + \frac{\beta}{2\varepsilon_0}\boldsymbol{D}^0 \cdot \boldsymbol{C}\boldsymbol{D}^0 \tag{41}$$

Here, $\mu$ is the initial shear modulus; $\beta = 1/\varepsilon_r$, where $\varepsilon_r$ is the relative permittivity related to the dielectric constant through $\varepsilon = \varepsilon_r \varepsilon_0$, with $\varepsilon_0$ is the vacuum permittivity. For the isotropic case, we use the dimensionless Eulerian electric displacement as $\widehat{D} = \lambda^{-2} D_0/\sqrt{\mu\varepsilon_0}$. The results are plotted for two different values of the electric displacement $\widehat{D} = 2$ (a), 2.4 (b) and electroelastic coupling parameter $\beta = 1/2$. The results coincide with the ones obtained by (Dorfmann and Ogden, 2014) for the isotropic dielectric plate under the same loading conditions.

Next, we illustrate the effect of the phase volume fraction on the plate stability. Fig. 6 shows the results for the DE composite plate with different volume fractions $c^{(f)} = 0.1$, 0.2,0.5 denoted by continuous, dashed, and short-dashed curves, respectively. The blue and red curves correspond to the antisymmetric and symmetric instability modes, respectively. The composite plates with the shear and dielectric modulus contrast ratios $\chi = 10$ and $\xi = 10$ are subjected to the electric excitation of the magnitude $\overline{D} = 2$. We observe that the DE composite plates with

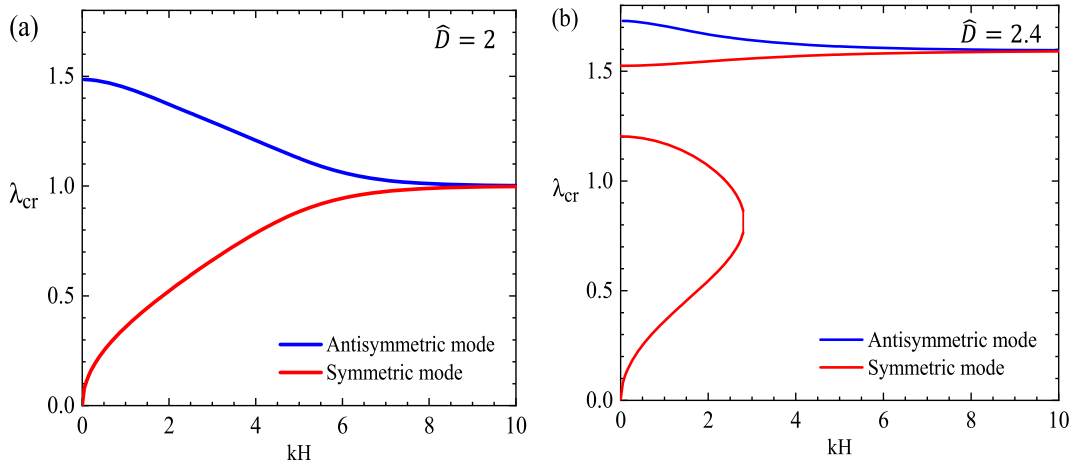


**Fig. 5.** The critical stretch versus the normalized wavenumber $kH$ for an equibiaxially stretched plate with flexible electrodes for the material model (41) with material parameter $\beta = 1/2$. The plate is subjected to two different levels of electric excitation $\widehat{D} = 2$ (a), and $\widehat{D} = 2.4$ (b) (Dorfmann and Ogden, 2014). The blue and red curves denote the antisymmetric and symmetric bifurcation modes, respectively. (For interpretation of the references to colour in this figure legend, the reader is referred to the Web version of this article.)

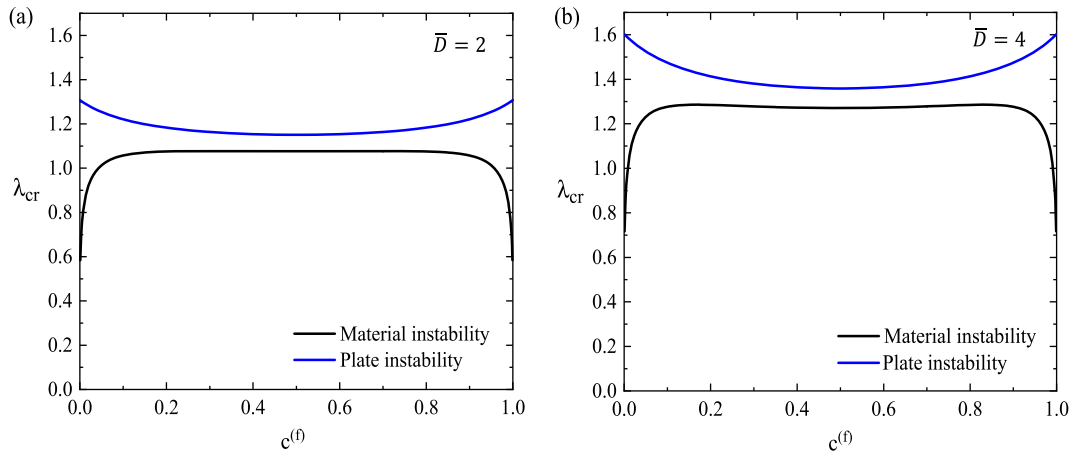


**Fig. 7.** The critical stretch versus the volume fraction of the stiffer phase $c^{(f)}$ for the DE laminate plate with $\chi = 10$, $\xi = 10$; the curves are shown for the longwave limit $kH \to 0$. The plate is subjected to two different levels of electric excitation: $\overline{D} = 2$ (a), and $\overline{D} = 4$ (b). The black and blue curves denote the macroscopic material, and plate instabilities, respectively. (For interpretation of the references to colour in this figure legend, the reader is referred to the Web version of this article.)

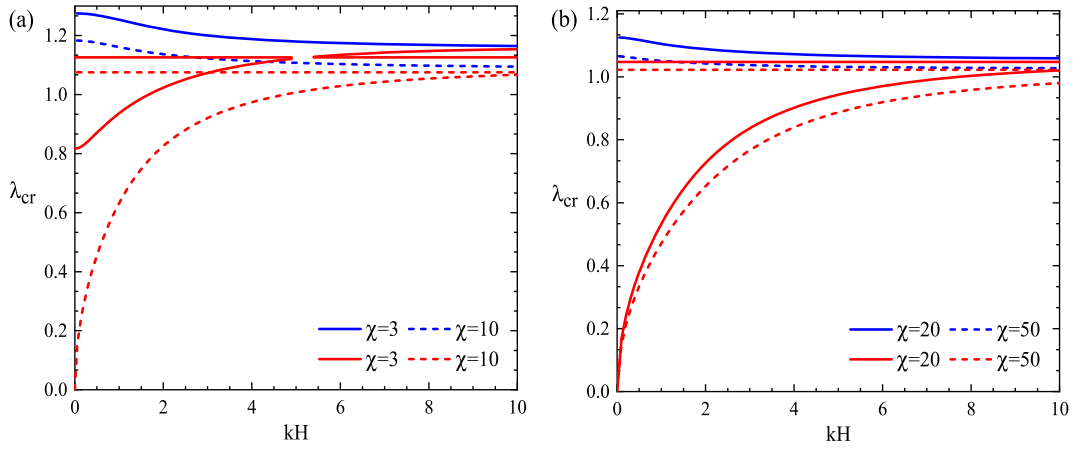


**Fig. 8.** The critical stretch versus the normalized wavenumber $kH$ for the DE laminate plate with $c^{(f)} = 0.2$, $\xi = 10$ and different shear moduli ratios $\chi = 3, 10$ (a), and $\chi = 20, 50$ (b). The plate is subjected to the electric excitation $\overline{D} = 2$. The blue and red curves denote the antisymmetric and symmetric bifurcation modes, respectively. (For interpretation of the references to colour in this figure legend, the reader is referred to the Web version of this article.)

low volume fractions of the stiffer phase are more prone to instabilities than those with higher volume fractions. We note that the effect of the phase volume fraction varies to the opposite effect for $c^{(f)} > 0.5$, and plates with higher volume fractions of the stiffer phase become more prone to instability development. As it can be observed from the figure, for $c^{(f)} < 0.1$, the symmetric bifurcation curve experiences a significant shape change.

Fig. 7 summarizes these results showing the critical stretch as the function of the stiff phase volume fraction. Note that the results are shown for the long-wave mode $kH \to 0$. Here, the results are displayed for the composites with the shear and dielectric modulus contrast ratios $\chi = 10$ and $\xi = 10$. The plates are subjected to $\overline{D} = 2$ (a) and $\overline{D} = 4$ (b). The black and blue curves correspond to the macroscopic material, and structural (plate) antisymmetric modes of instability, respectively.

We observe that for $\overline{D} = 2$, the macroscopic material instabilities appear earlier than the structural plate instabilities. The macroscopic instability curve increases monotonically for volume fractions up to $c^{(f)} = 0.29$ and then continues to lower critical stretches with an increase in the volume fraction up to $c^{(f)} = 0.5$. This effect varies to the opposite effect for $c^{(f)} > 0.5$. For $\overline{D} = 4$, the material instability curve increases for volume fractions up to $c^{(f)} = 0.17$, then decreases to lower critical stretches until $c^{(f)} = 0.5$. Moreover, the antisymmetric unstable domain decreases with an increase in the volume fraction up to $c^{(f)} = 0.5$, and increases with an increase in the volume fraction for $c^{(f)} > 0.5$. The curves are symmetric with respect to $c^{(f)} = 0.5$, and the trend of the curves is reversed for plates with higher stiffer phase volume fractions.

Next, we examine the influence of the phase shear moduli contrast ratio on the instabilities in the composite dielectric plates. Fig. 8 shows the dependence of the critical stretch on the normalized wavenumber $kH$ for the DE composite plates with various shear moduli ratios $\chi = 3, 10$ (denoted by continuous, and dashed curves, respectively) in Fig. 8(a), and $\chi = 20, 50$ (denoted by continuous, and dashed curves, respectively) in Fig. 8(b). The blue and red curves correspond to the antisymmetric and symmetric instability modes, respectively. The plate with the volume fraction of the stiffer phase $c^{(f)} = 0.2$ and contrast ratio $\xi = 10$ is subjected to electrical excitation $\overline{D} = 2$. The diagrams show that with an increase in the shear moduli ratio, the critical stretch decreases. Furthermore, for values of $\chi = 3$ and less, the shape of the symmetric bifurcation curve changes, and two different symmetric modes appear (instead of a single curve for the cases with higher levels of the shear moduli ratio). The upper instability curve has its maximum at $kH \to 0$, and it gradually decreases as the normalized wavenumber increases. Fig. 8(b) shows that, at large enough contrasts, the variation of the critical stretch with respect to the normalized wavenumber is much less than that at low contrasts. For example, for the composite with $\chi = 50$

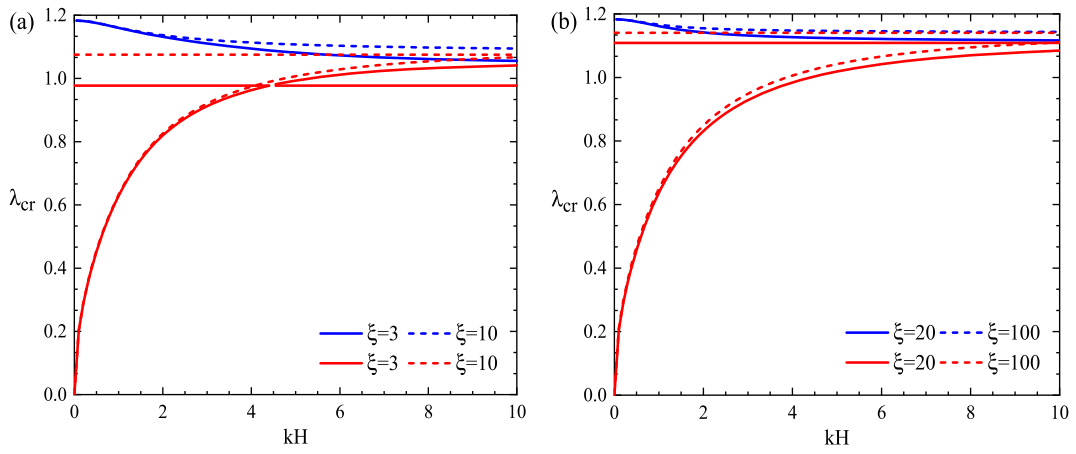


**Fig. 9.** The critical stretch versus the normalized wavenumber $kH$ for the DE laminate plate with $c^{(f)} = 0.2$, $\chi = 10$ and different permittivity ratios $\xi = 3, 10$ (a), and $\xi = 20, 100$ (b). The plate is subjected to the electric excitation $\overline{D} = 2$. The blue and red curves correspond to the antisymmetric and symmetric bifurcation modes, respectively. (For interpretation of the references to colour in this figure legend, the reader is referred to the Web version of this article.)

the change of the critical stretch ratios is $1.028 < \lambda_{cr} < 1.065$ in the entire range of $kH$.

Fig. 9 illustrates the evaluations of unstable domains with the phase dielectric constant ratio. The results are shown for the DE composite plates with $c^{(f)} = 0.2$, $\chi = 10$, and $\xi = 3, 10$ (denoted by continuous, and dashed curves, respectively) in Fig. 9(a), and $\xi = 20, 100$ (denoted by continuous, and dashed curves, respectively) in Fig. 9(b). The DE composite plate is subjected to the electric excitation $\overline{D} = 2$. We observe that an increase in the permittivity ratio results in an increase in the critical stretch for both antisymmetric and symmetric instability modes for wavenumbers $kH > 0$. We note, however, that the antisymmetric critical stretch corresponding to $kH \to 0$ does not change with a change in the dielectric constant contrast; for the considered cases the critical stretch ratio is $\lambda_{cr} \approx 1.183$. This seemingly counterintuitive result stems from the normalization of the applied electric displacement; the *actual* applied electric displacement changes with a change in the dielectric contrast (when the normalized electric displacement value is fixed). The dependence is illustrated by considering the actual electric displacement (normalized by the matrix properties) in Appendix B. Also, a shape change in the symmetric bifurcation curve is shown in Fig. 9(a) for the phase dielectric constant ratio $\xi = 3$. We can observe the instability curves get close to each other for the composites with high dielectric constants ratios (see the continuous and dashed curves corresponding to $\xi = 20$ and 100, respectively, in Fig. 9(b)).

In Fig. 10, we plot the dependence of the critical stretches on the phase contrasts such that the contrasts in shear moduli and electric permittivities are identical, namely, $\chi = \xi$. The results are shown for the long-wave limit $kH \to 0$. The black and blue curves represent the material and plate (antisymmetric modes) instabilities, respectively. The examples are given for the DE laminates with $c^{(f)} = 0.03$ in Fig. 10(a) and $c^{(f)} = 0.5$ in Fig. 10(b), and subjected to $\overline{D} = 2$ and 4. We observe that an increase in the phase contrasts leads to a decrease in the plate critical stretch, whereas the critical stretch (corresponding to the material instability) increases for composites with lower contrasts between the properties of the phases, and then decreases for composites with higher contrasts. Note that for the laminate with $c^{(f)} = 0.03$ the material stability criterion predicts similar critical stretch values as the structural plate intability analysis for high enough contrast ratios, $\chi = \xi$ larger than ≈300. The curve of the material instability branches from the curve of the plate instability in a large range of contrast ratios (up to $\chi = \xi \approx 300$). For the DE composite plate with $c^{(f)} = 0.5$, the predictions of the two failure criteria are close to each other at contrasts smaller than those for the DE plate with $c^{(f)} = 0.03$ (see Fig. 10(b)). The bifurcation

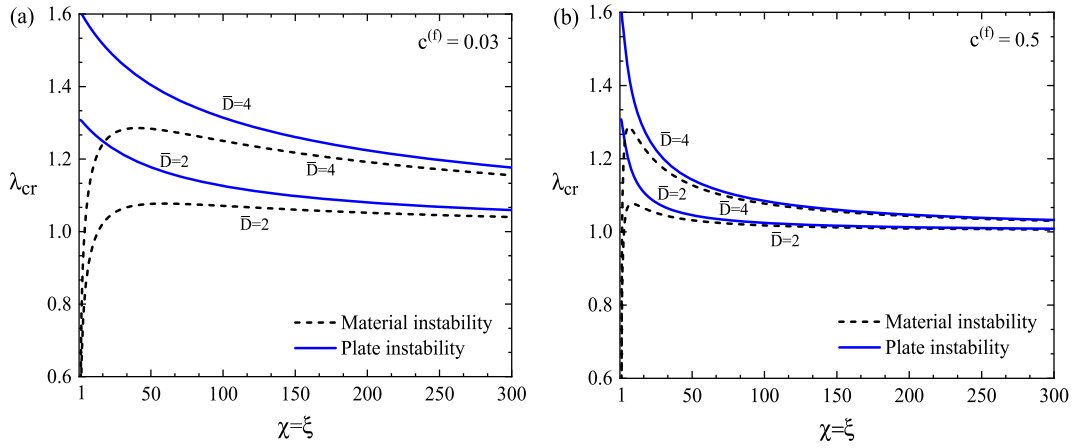


**Fig. 10.** The critical stretch versus the phase contrasts $\chi = \xi$ for the DE laminate plate with $c^{(f)} = 0.03$ (a), and $c^{(f)} = 0.5$ (b) when $kH \to 0$. The plate is subjected to two different levels of the electric excitation: $\overline{D} = 2$ and 4. The black and blue curves denote the macroscopic material, and plate instabilities, respectively. (For interpretation of the references to colour in this figure legend, the reader is referred to the Web version of this article.)

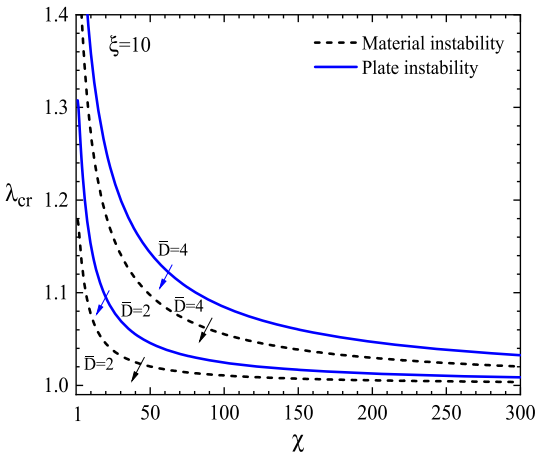


**Fig. 11.** The critical stretch versus the shear moduli ratio and $\xi = 10$, for the DE laminate plate with $c^{(f)} = 0.5$, and when $kH \to 0$. The plate is subjected to two different levels of the electric excitation: $\overline{D} = 2$ and 4. The black and blue curves denote the macroscopic material, and plate instabilities, respectively. (For interpretation of the references to colour in this figure legend, the reader is referred to the Web version of this article.)

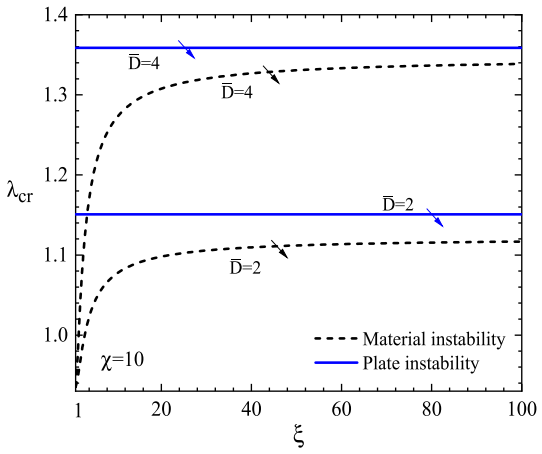


**Fig. 12.** The critical stretch versus the dielectric constants ratio and $\chi = 10$, for the DE laminate plate with $c^{(f)} = 0.5$, and when $kH \to 0$. The plate is subjected to two different levels of the electric excitation: $\overline{D} = 2$ and 4. The black and blue curves denote the material, and antisymmetric modes of instability, respectively. (For interpretation of the references to colour in this figure legend, the reader is referred to the Web version of this article.)

curve based on the plate stability criterion approaches the one predicted by the material criterion for contrast values beyond $\chi = \xi \approx 50$.

In Fig. 11, we compare the instability criterion predictions for DE laminates plates with a fixed dielectric constant ratio and varying shear modulus contrast ratio. The results are shown for the longwave case $kH \to 0$. The black and blue curves represent the macroscopic material, and structural antisymmetric instability modes, respectively. The examples are given for the DE laminate plate with $c^{(f)} = 0.5$, subjected to $\overline{D} = 2$ and 4. Fig. 11 shows the dependence of the critical stretch on the shear moduli ratio with the fixed dielectric constant ratio $\xi = 10$. As it is shown, the critical stretch increases when the electric displacement field goes up, which means the electric displacement has a destabilizing effect. The results show that the material instability curves are lower than their plate instability counterparts. Hence, the stable range of $\lambda_{cr}$ is determined by the area above the blue curve. It is observed that the structural and material instability curves are monotonically decreasing functions of $\chi$ for the two values of the electric displacement. For $\overline{D} = 2$, the two criteria predict similar critical stretches for the DE laminates with high shear modulus ratios. For example, the material criterion predicts the onset of instability at $\lambda_{cr} = 1.004$ for $\chi = 300$, while the plate instability develops at $\lambda_{cr} = 1.009$. The difference predicted by the two criteria increases as the shear moduli ratio decreases. For an increased excitation level, $\overline{D} = 4$, the curves approach each other at high levels of the shear modulus contrasts. For example, for $\chi = 400$, the critical stretch values based on the material and plate criteria are respectively $\lambda_{cr} = 1.015$ and $\lambda_{cr} = 1.025$.

Finally, we compare the material and plate instability predictions in DE laminate plates with a fixed shear modulus ratio and varying dielectric constant ratio. Fig. 12 shows the example for the DE composite plate with $c^{(f)} = 0.5$ and the fixed shear moduli ratio $\chi = 10$; the plate is subjected to the electric excitations $\overline{D} = 2$ and $\overline{D} = 4$. In agreement with the previous observations, the plate instability curves are above the corresponding material instability ones. We note that the critical stretches of the plate instability antisymmetric mode are independent of the dielectric contrast ratio at given normalized electric displacement levels; in particular, $\lambda_{cr} = 1.151$ for $\overline{D} = 2$, and $\lambda_{cr} = 1.359$ for $\overline{D} = 4$. Recall that this is due to the normalization of the applied electric displacement (the dependence of the critical stretch on the actual electric displacement is given in Appendix B). The critical stretches of the macroscopic material instability, however, initially show their strong dependence on the dielectric constant ratio followed by their asymptotic behavior towards the corresponding critical stretch values. Thus, the materials critical stretch ratios attain $\lambda_{cr} = 1.121$ at $\overline{D} = 2$, and $\lambda_{cr} = 1.345$ at $\overline{D} = 4$.

## 6. Conclusion

We examined the instability of dielectric composite plates that may occur at (i) structural plate level and (ii) microstructural material level. We considered the elastomer plates with layered microstructure with ideal dielectric incompressible phases; the composite DE plates are subjected to finite deformations and electric fields. In the plate structural instability analysis, decoupled equations associated with antisymmetric (flexural) and symmetric (barrelling) modes were obtained. We investigated the influence of the electro-mechanical loading, and microstructural parameters on the stability of DE composites. We observed that the application of the electric field results in destabilizing the dielectric composite plates. We found that in the composite plates with small volume fractions of the active phase, an increase in the stiffer phase volume fraction results in a decrease in the critical stretch. However, in the composite plates with a high volume fraction of the active stiffer phase, an increase in the volume fraction has a destabilizing effect (the critical stretch increases). We compared the results of the plate structural instability analysis with the prediction of material instabilities (based on the macroscopic instability analysis) for the limiting case $kH \to 0$. The instability predictions of the plate and material criteria were examined for a large range of the shear moduli and dielectric constant ratios for the longwave case $kH \to 0$. The two criteria predict close values for DE laminate plates with high shear moduli contrasts. In addition, the stabilizing effect of the shear moduli ratio on the onset of structural instabilities was demonstrated. DE laminate plates with higher dielectric constant ratios are found to be more prone to instability development. Overall, the closed-form material instability estimate may be used for predicting instabilities in DE laminate plates with relatively high contrasts in the phase properties. For the laminate plates with lower contrasts in the constituent properties, the involving plate instability analysis is needed to obtain accurate predictions for the onset of instability.

## Author statement

Marzieh Bahreman led to the mathematical model development and

numerical implementation. Nitesh Arora contributed to the research development and analysis. Stephan Rudykh developed the idea and oversaw the research. All authors (Marzieh Bahreman, Nitesh Arora, Hossein Darijani, and Stephan Rudykh) discussed the research and participated in the manuscript composition and discussion.

## Declaration of competing interest

The authors declare that they have no known competing financial interests or personal relationships that could have appeared to influence the work reported in this paper.

## Acknowledgements

NA acknowledge the support through LeRoy fellowship. SR is grateful for the support of European Research Council (ERC) through Grant No. 852281 - MAGIC.

## Appendix A. Analytical explicit expressions for roots of Eq. (29)

Here, we give expressions for the analytical solution of Eq. (29). Rewriting this equation as

$$z_1 s^6 - z_2 s^4 + z_3 s^2 - z_4 = 0$$

where

$$z_1 = cf - d^2, \quad z_2 = 2bf + cg + 2(d-e)d$$

$$z_3 = 2bg + af - (d-e)^2, \quad z_4 = ag$$

and, taking $t = s^2$ we will have

$$z_1 t^3 - z_2 t^2 + z_3 t - z_4 = 0$$

Solving this cubic equation, one can obtain the corresponding roots as follow

$$s_1 = -s_4 = \frac{\sqrt{3}}{3}\left[2\sqrt{-3\frac{z_3}{z_1} + \left(\frac{z_2}{z_1}\right)^2}\, sin\left(\frac{1}{3}sin^{-1}\left(\frac{81}{2}\frac{\sqrt{3}\left(-\frac{2}{27}\left(\frac{z_2}{z_1}\right)^3 + \frac{1}{3}\frac{z_2 z_3}{z_1^2} - \frac{z_4}{z_1}\right)}{\left(-9\frac{z_3}{z_1} + 3\left(\frac{z_2}{z_1}\right)^2\right)^{\frac{3}{2}}}\right)\right) + \frac{z_2}{z_1}\right]^{\frac{1}{2}}$$

$$s_2 = -s_5 = \frac{\sqrt{3}}{3}\left[-2\sqrt{-3\frac{z_3}{z_1} + \left(\frac{z_2}{z_1}\right)^2}\, sin\left(\frac{1}{3}sin^{-1}\left(\frac{81}{2}\frac{\sqrt{3}\left(-\frac{2}{27}\left(\frac{z_2}{z_1}\right)^3 + \frac{1}{3}\frac{z_2 z_3}{z_1^2} - \frac{z_4}{z_1}\right)}{\left(-9\frac{z_3}{z_1} + 3\left(\frac{z_2}{z_1}\right)^2\right)^{\frac{3}{2}}}\right) + \frac{\pi}{3}\right) + \frac{z_2}{z_1}\right]^{\frac{1}{2}}$$

$$s_3 = -s_6 = \frac{\sqrt{3}}{3}\left[2\sqrt{-\frac{z_3}{z_1} + \left(\frac{z_2}{z_1}\right)^2}\, cos\left(\frac{1}{3}sin^{-1}\left(\frac{81}{2}\frac{\sqrt{3}\left(-\frac{2}{27}\left(\frac{z_2}{z_1}\right)^3 + \frac{1}{3}\frac{z_2 z_3}{z_1^2} - \frac{z_4}{z_1}\right)}{\left(-9\frac{z_3}{z_1} + 3\left(\frac{z_2}{z_1}\right)^2\right)^{\frac{3}{2}}}\right) + \frac{\pi}{6}\right) + \frac{z_2}{z_1}\right]^{\frac{1}{2}}$$

in which $\frac{z_2}{z_1}$, $\frac{z_3}{z_1}$ and $\frac{z_4}{z_1}$ are obtained introducing the material coefficients (36) as

$$\frac{z_2}{z_1} = \left(\lambda^6 + 3\right)\frac{\overline{\mu}}{\breve{\mu}} + \frac{\overline{\varepsilon}}{\breve{\varepsilon}} - 2$$

$$\frac{z_3}{z_1} = \left[\left(\lambda^6 + 3\right)\frac{\overline{\varepsilon}}{\breve{\varepsilon}} + \left(\lambda^6 - 1\right)\right]\frac{\overline{\mu}}{\breve{\mu}} + \left[1 - \frac{\overline{\varepsilon}}{\breve{\varepsilon}}\right]\overline{D}^2 - 2\frac{\overline{\varepsilon}}{\breve{\varepsilon}} + 1$$

$$\frac{z_4}{z_1} = \left[\left(\lambda^6 - 1\right)\frac{\overline{\mu}}{\breve{\mu}} + 1\right]\frac{\overline{\varepsilon}}{\breve{\varepsilon}} + \left[1 - \frac{\overline{\varepsilon}}{\breve{\varepsilon}}\right]\overline{D}^2$$

## Appendix B. Effect of dielectric constant ratio on the onset of instabilities

Here, we illustrate the effect of the permittivity ratio on the onset of instabilities considering the actual electric displacement $D^* = \overline{D}^0/\sqrt{\mu^{(m)}\varepsilon^{(m)}}$ (normalized by the matrix properties). Using this normalization for the electric displacement, we show in Fig. 13 that the dielectric constant ratio has a decreasing effect on the onset of bifurcation. This is unlike what we observed in Fig. 9 in which for $kH \to 0$, the critical stretch value was the same for different contrasts. Rewriting the normalized displacement $\overline{D} = \overline{D}^0/\sqrt{\breve{\mu}\breve{\varepsilon}}$ in terms of $D^*$ and the contrast $\xi$, we displayed the variation of the actual

electric displacement with respect to the permittivity ratio by the red curved in Fig. 13. The curve is plotted for the laminate plates with $c^{(f)} = 0.2, \chi = 10$, and $\overline{D} = 2$. It is observed that the actual field increases with increase in the permittivity ratio. Moreover, the dependence of the plate critical stretch on the contrast in electric permittivities for the long-wave mode $kH \to 0$ is illustrated by the blue curve in Fig. 13. The results are shown for the DE laminate plate with $c^{(f)} = 0.2, \chi = 10$; the DE laminate plate is subjected to the electric displacement $D^* = 2$. It is found that the onset of structural instabilities is dependent on the dielectric constant ratio; it decreases as the dielectric constant ratio increases.

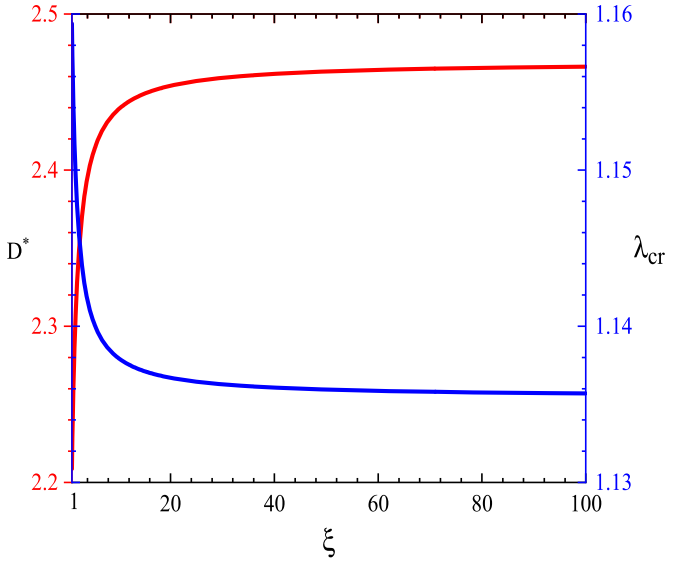


**Fig. 13.** The actual electric displacement $D^*$ versus the dielectric constants ratio for the plate with $c^{(f)} = 0.2, \chi = 10$, and $\overline{D} = 2$ (red curve), and the critical stretch versus dielectric constants ratio for the DE laminate plate with $c^{(f)} = 0.2$, $\chi = 10$, and when $kH \to 0$. The plate is subjected to the electric excitation $D^* = 2$ (blue curve).

## References


Aboudi, J., 2015. Micro-electromechanics of soft dielectric matrix composites. Int. J. Solid Struct. 64, 30–41.

Arora, N., Batan, A., Li, J., Slesarenko, V., Rudykh, S., 2019. On the influence of inhomogeneous interphase layers on instabilities in hyperelastic composites. Materials 12, 763.

Arora, N., Kumar, P., Joglekar, M., 2018. A modulated voltage waveform for enhancing the travel range of dielectric elastomer actuators. J. Appl. Mech. 85.

Arora, N., Li, J., Slesarenko, V., Rudykh, S., 2020. Microscopic and long-wave instabilities in 3D fiber composites with non-Gaussian hyperelastic phases. Int. J. Eng. Sci. 157, 103408.

Babaee, S., Viard, N., Wang, P., Fang, N.X., Bertoldi, K., 2016. Harnessing deformation to switch on and off the propagation of sound. Adv. Mater. 28, 1631–1635.

Bertoldi, K., Boyce, M., 2008. Mechanically triggered transformations of phononic band gaps in periodic elastomeric structures. Phys. Rev. B 77, 052105.

Bertoldi, K., Gei, M., 2011. Instabilities in multilayered soft dielectrics. J. Mech. Phys. Solid. 59, 18–42.

Bertoldi, K., Lopez-Pamies, O., 2012. Some remarks on the effect of interphases on the mechanical response and stability of fiber-reinforced elastomers. J. Appl. Mech. 79.

Biddiss, E., Chau, T., 2008. Dielectric elastomers as actuators for upper limb prosthetics: challenges and opportunities. Med. Eng. Phys. 30, 403–418.

Blok, J., LeGrand, D., 1969. Dielectric breakdown of polymer films. J. Appl. Phys. 40, 288–293.

Brochu, P., Pei, Q., 2012. Dielectric Elastomers for Actuators and Artificial Muscles, Electroactivity in Polymeric Materials. Springer, pp. 1–56.

Broderick, H.C., Righi, M., Destrade, M., Ogden, R.W., 2020. Stability analysis of charge-controlled soft dielectric plates. Int. J. Eng. Sci. 151, 103280.

Carpi, F., Bauer, S., De Rossi, D., 2010. Stretching dielectric elastomer performance. Science 330, 1759–1761.

Carpi, F., Salaris, C., De Rossi, D., 2007. Folded dielectric elastomer actuators. Smart Mater. Struct. 16, S300.

Chakraborti, P., Toprakci, H.K., Yang, P., Di Spigna, N., Franzon, P., Ghosh, T., 2012. A compact dielectric elastomer tubular actuator for refreshable Braille displays. Sensor Actuator Phys. 179, 151–157.

De Tommasi, D., Puglisi, G., Saccomandi, G., Zurlo, G., 2010. Pull-in and wrinkling instabilities of electroactive dielectric actuators. J. Phys. Appl. Phys. 43, 325501.

De Tommasi, D., Puglisi, G., Zurlo, G., 2011. Compression-induced failure of electroactive polymeric thin films. Appl. Phys. Lett. 98, 123507.

Dehghani, H., Desena-Galarza, D., Jha, N., Reinoso, J., Merodio, J., 2019. Bifurcation and post-bifurcation of an inflated and extended residually-stressed circular cylindrical tube with application to aneurysms initiation and propagation in arterial wall tissue. Finite Elem. Anal. Des. 161, 51–60.

Díaz-Calleja, R., Sanchis, M., Riande, E., 2009. Effect of an electric field on the bifurcation of a biaxially stretched incompressible slab rubber. Eur. Phys. J. E 30, 417.

Dorfmann, A., Ogden, R., 2005. Nonlinear electroelasticity. Acta Mech. 174, 167–183.

Dorfmann, A., Ogden, R.W., 2010. Nonlinear electroelastostatics: incremental equations and stability. Int. J. Eng. Sci. 48, 1–14.

Dorfmann, L., Ogden, R.W., 2014. Instabilities of an electroelastic plate. Int. J. Eng. Sci. 77, 79–101.

Dorfmann, L., Ogden, R.W., 2019. Instabilities of soft dielectrics. Philos. Trans. Roy. Soc. A 377, 20180077.

El Hamdaoui, M., Merodio, J., Ogden, R., 2020. Two-phase piecewise homogeneous plane deformations of a fibre-reinforced neo-Hookean material with application to fibre kinking and splitting. J. Mech. Phys. Solid. 143, 104091.

El Hamdaoui, M., Merodio, J., Ogden, R.W., 2015. Loss of ellipticity in the combined helical, axial and radial elastic deformations of a fibre-reinforced circular cylindrical tube. Int. J. Solid Struct. 63, 99–108.

Fang, Z.H., Punckt, C., Leung, E.Y., Schniepp, H.C., Aksay, I.A., 2010. Tuning of structural color using a dielectric actuator and multifunctional compliant electrodes. Appl. Opt. 49, 6689–6696.

Galich, P.I., Rudykh, S., 2017. Shear wave propagation and band gaps in finitely deformed dielectric elastomer laminates: long wave estimates and exact solution. J. Appl. Mech. 84.

Gei, M., Roccabianca, S., Bacca, M., 2010. Controlling bandgap in electroactive polymer-based structures. IEEE ASME Trans. Mechatron. 16, 102–107.

Goshkoderia, A., Arora, N., Slesarenko, V., Li, J., Chen, V., Juhl, A., Buskohl, P., Rudykh, S., 2020. Tunable permittivity in dielectric elastomer composites under finite strains: periodicity, randomness, and instabilities. Int. J. Mech. Sci. 186, 105880.

Goshkoderia, A., Rudykh, S., 2017. Electromechanical macroscopic instabilities in soft dielectric elastomer composites with periodic microstructures. Eur. J. Mech. Solid. 65, 243–256.

Gu, G.-Y., Zhu, J., Zhu, L.-M., Zhu, X., 2017. A survey on dielectric elastomer actuators for soft robots. Bioinspiration Biomimetics 12, 011003.

Huang, C., Zhang, Q., 2004. Enhanced dielectric and electromechanical responses in high dielectric constant all-polymer percolative composites. Adv. Funct. Mater. 14, 501–506.

Itskov, M., Khiêm, V.N., 2016. A polyconvex anisotropic free energy function for electro- and magneto-rheological elastomers. Math. Mech. Solid 21, 1126–1137.

Jabareen, M., 2015. On the modeling of electromechanical coupling in electroactive polymers using the mixed finite element formulation. Procedia IUTAM 12, e115.

Keip, M.-A., Steinmann, P., Schröder, J., 2014. Two-scale computational homogenization of electro-elasticity at finite strains. Comput. Methods Appl. Mech. Eng. 278, 62–79.

Keplinger, C., Li, T., Baumgartner, R., Suo, Z., Bauer, S., 2012. Harnessing snap-through instability in soft dielectrics to achieve giant voltage-triggered deformation. Soft Matter 8, 285–288.

Koh, S.J.A., Keplinger, C., Li, T., Bauer, S., Suo, Z., 2010. Dielectric elastomer generators: how much energy can be converted? IEEE/ASME Trans. Mech. 16, 33–41.
Kolle, M., Lethbridge, A., Kreysing, M., Baumberg, J.J., Aizenberg, J., Vukusic, P., 2013. Bio-inspired band-gap tunable elastic optical multilayer fibers. Adv. Mater. 25, 2239–2245.
Lee, H., Fang, N.X., 2012. Micro 3D printing using a digital projector and its application in the study of soft materials mechanics. JoVE e4457.
Li, J., Arora, N., Rudykh, S., 2021. Elastic instabilities, microstructure transformations, and pattern formations in soft materials. Curr. Opin. Solid State Mater. Sci. 25, 100898.
Li, J., Pallicity, T.D., Slesarenko, V., Goshkoderia, A., Rudykh, S., 2019. Domain formations and pattern transitions via instabilities in soft heterogeneous materials. Adv. Mater. 31, 1807309.
Li, J., Slesarenko, V., Galich, P.I., Rudykh, S., 2018a. Instabilities and pattern formations in 3D-printed deformable fiber composites. Compos. B Eng. 148, 114–122.
Li, J., Slesarenko, V., Rudykh, S., 2018b. Auxetic multiphase soft composite material design through instabilities with application for acoustic metamaterials. Soft Matter 14, 6171–6180.
Li, T., Qu, S., Yang, W., 2012. Electromechanical and dynamic analyses of tunable dielectric elastomer resonator. Int. J. Solid Struct. 49, 3754–3761.
Liu, L., 2013. On energy formulations of electrostatics for continuum media. J. Mech. Phys. Solid. 61, 968–990.
Liu, X., Li, B., Chen, H., Jia, S., Zhou, J., 2016. Voltage-induced wrinkling behavior of dielectric elastomer. J. Appl. Polym. Sci. 133.
Mao, G., Hong, W., Kaltenbrunner, M., Qu, S., 2021. A numerical approach based on finite element method for the wrinkling analysis of dielectric elastomer membranes. J. Appl. Mech. 1–37.
McMeeking, R.M., Landis, C.M., 2005. Electrostatic Forces and Stored Energy for Deformable Dielectric Materials.
Mehnert, M., Hossain, M., Steinmann, P., 2019. Experimental and numerical investigations of the electro-viscoelastic behavior of VHB 4905TM. Eur. J. Mech. Solid. 77, 103797.
Melnikov, A., Ogden, R.W., Dorfmann, L., Merodio, J., 2021. Bifurcation analysis of elastic residually-stressed circular cylindrical tubes. Int. J. Solid Struct. 226, 111062.
Merodio, J., Ogden, R., 2003. Instabilities and loss of ellipticity in fiber-reinforced compressible non-linearly elastic solids under plane deformation. Int. J. Solid Struct. 40, 4707–4727.
Merodio, J., Ogden, R., 2005a. On tensile instabilities and ellipticity loss in fiber-reinforced incompressible non-linearly elastic solids. Mech. Res. Commun. 32, 290–299.
Merodio, J., Ogden, R., 2005b. Remarks on instabilities and ellipticity for a fiber-reinforced compressible nonlinearly elastic solid under plane deformation. Q. Appl. Math. 63, 325–333.
Merodio, J., Ogden, R., 2005c. Tensile instabilities and ellipticity in fiber-reinforced compressible non-linearly elastic solids. Int. J. Eng. Sci. 43, 697–706.
Nam, N., Merodio, J., Ogden, R., Vinh, P., 2016. The effect of initial stress on the propagation of surface waves in a layered half-space. Int. J. Solid Struct. 88, 88–100.
Ortigosa, R., Gil, A.J., 2016. A new framework for large strain electromechanics based on convex multi-variable strain energies: conservation laws, hyperbolicity and extension to electro-magneto-mechanics. Comput. Methods Appl. Mech. Eng. 309, 202–242.
Park, H.S., Suo, Z., Zhou, J., Klein, P.A., 2012. A dynamic finite element method for inhomogeneous deformation and electromechanical instability of dielectric elastomer transducers. Int. J. Solid Struct. 49, 2187–2194.
Pelrine, R., Kornbluh, R., Joseph, J., Heydt, R., Pei, Q., Chiba, S., 2000a. High-field deformation of elastomeric dielectrics for actuators. Mater. Sci. Eng. C 11, 89–100.
Pelrine, R., Kornbluh, R., Pei, Q., Joseph, J., 2000b. High-speed electrically actuated elastomers with strain greater than 100. Science 287, 836–839.
Pelrine, R.E., Kornbluh, R.D., Joseph, J.P., 1998. Electrostriction of polymer dielectrics with compliant electrodes as a means of actuation. Sensor Actuator Phys. 64, 77–85.
Plante, J.-S., Dubowsky, S., 2006. Large-scale failure modes of dielectric elastomer actuators. Int. J. Solid Struct. 43, 7727–7751.
Polukhov, E., Vallicotti, D., Keip, M.-A., 2018. Computational stability analysis of periodic electroactive polymer composites across scales. Comput. Methods Appl. Mech. Eng. 337, 165–197.
Rodríguez, J., Merodio, J., 2016. Helical buckling and postbuckling of pre-stressed cylindrical tubes under finite torsion. Finite Elem. Anal. Des. 112, 1–10.
Rudykh, S., Bhattacharya, K., deBotton, G., 2012. Snap-through actuation of thick-wall electroactive balloons. Int. J. Non Lin. Mech. 47, 206–209.
Rudykh, S., Bhattacharya, K., DeBotton, G., 2014. Multiscale instabilities in soft heterogeneous dielectric elastomers. Proc. Math. Phys. Eng. Sci. 470, 20130618.
Rudykh, S., Boyce, M.C., 2014. Transforming wave propagation in layered media via instability-induced interfacial wrinkling. Phys. Rev. Lett. 112, 034301.
Rudykh, S., Debotton, G., 2011. Stability of anisotropic electroactive polymers with application to layered media. Z. Angew. Math. Phys. 62, 1131–1142.
Rudykh, S., deBotton, G., 2012. Instabilities of hyperelastic fiber composites: micromechanical versus numerical analyses. J. Elasticity 106, 123–147.
Rudykh, S., Lewinstein, A., Uner, G., deBotton, G., 2013. Analysis of microstructural induced enhancement of electromechanical coupling in soft dielectrics. Appl. Phys. Lett. 102, 151905.
Sharma, A.K., Arora, N., Joglekar, M., 2018. DC dynamic pull-in instability of a dielectric elastomer balloon: an energy-based approach. Proc. Math. Phys. Eng. Sci. 474, 20170900.
Sharma, A.K., Joglekar, M., 2019a. A computationally efficient locking free numerical framework for modeling visco-hyperelastic dielectric elastomers. Comput. Methods Appl. Mech. Eng. 352, 625–653.
Sharma, A.K., Joglekar, M., 2019b. A numerical framework for modeling anisotropic dielectric elastomers. Comput. Methods Appl. Mech. Eng. 344, 402–420.
Sharma, A.K., Kumar, P., Singh, A., Joglekar, D., Joglekar, M., 2019. Electromechanical instability of dielectric elastomer actuators with active and inactive electric regions. J. Appl. Mech. 86.
Slesarenko, V., Rudykh, S., 2017. Microscopic and macroscopic instabilities in hyperelastic fiber composites. J. Mech. Phys. Solid. 99, 471–482.
Spinelli, S.A., Lopez-Pamies, O., 2015. Some simple explicit results for the elastic dielectric properties and stability of layered composites. Int. J. Eng. Sci. 88, 15–28.
Stark, K., Garton, C., 1955. Electric strength of irradiated polythene. Nature 176, 1225–1226.
Stoyanov, H., Kollosche, M., Risse, S., McCarthy, D.N., Kofod, G., 2011. Elastic block copolymer nanocomposites with controlled interfacial interactions for artificial muscles with direct voltage control. Soft Matter 7, 194–202.
Su, Y., Broderick, H.C., Chen, W., Destrade, M., 2018. Wrinkles in soft dielectric plates. J. Mech. Phys. Solid. 119, 298–318.
Suo, Z., 2010. Theory of dielectric elastomers. Acta Mech. Solida Sin. 23, 549–578.
Suo, Z., Zhao, X., Greene, W.H., 2008. A nonlinear field theory of deformable dielectrics. J. Mech. Phys. Solid. 56, 467–486.
Tian, L., Tevet-Deree, L., DeBotton, G., Bhattacharya, K., 2012. Dielectric elastomer composites. J. Mech. Phys. Solid. 60, 181–198.
Toupin, R., 1960. Stress Tensors in Elastic Dielectrics.
Toupin, R.A., 1956. The elastic dielectric. J. Ration. Mech. Anal. 5, 849–915.
Triantafyllidis, N., Maker, B., 1985. On the Comparison between Microscopic and Macroscopic Instability Mechanisms in a Class of Fiber-Reinforced Composites.
Triantafyllidis, N., Nestorović, M., Schraad, M., 2006. Failure Surfaces for Finitely Strained Two-phase Periodic Solids under General In-Plane Loading.
Vu, D., Steinmann, P., Possart, G., 2007. Numerical modelling of non-linear electroelasticity. Int. J. Numer. Methods Eng. 70, 685–704.
Xu, B.-X., Mueller, R., Klassen, M., Gross, D., 2010. On electromechanical stability analysis of dielectric elastomer actuators. Appl. Phys. Lett. 97, 162908.
Zeng, C., Gao, X., 2020. Stability of an Anisotropic Dielectric Elastomer Plate. International Journal of Non-Linear Mechanics, p. 103510.
Zhao, X., Hong, W., Suo, Z., 2007. Electromechanical hysteresis and coexistent states in dielectric elastomers. Phys. Rev. B 76, 134113.
Zhao, X., Suo, Z., 2007. Method to analyze electromechanical stability of dielectric elastomers. Appl. Phys. Lett. 91, 061921.
Zhao, X., Suo, Z., 2010. Theory of dielectric elastomers capable of giant deformation of actuation. Phys. Rev. Lett. 104, 178302.
Zheng, X., Lee, H., Weisgraber, T.H., Shusteff, M., DeOtte, J., Duoss, E.B., Kuntz, J.D., Biener, M.M., Ge, Q., Jackson, J.A., 2014. Ultralight, ultrastiff mechanical metamaterials. Science 344, 1373–1377.
Zhu, J., Stoyanov, H., Kofod, G., Suo, Z., 2010. Large deformation and electromechanical instability of a dielectric elastomer tube actuator. J. Appl. Phys. 108, 074113.
Zurlo, G., Destrade, M., DeTommasi, D., Puglisi, G., 2017. Catastrophic thinning of dielectric elastomers. Phys. Rev. Lett. 118, 078001.